



Review

Analysis of the electrochemical performance of MoNi–CeO₂ cermet as anode material for solid oxide fuel cell. Part I. H₂, CH₄ and H₂/CH₄ mixtures as fuels

M.J. Escudero^{a,*}, I. Gómez de Parada^b, A. Fuerte^a, J.L. Serrano^a^a CIEMAT, Av. Complutense 40, 28040 Madrid, Spain^b UAM, Campus Cantoblanco, 28049 Madrid, Spain

H I G H L I G H T S

- MoNi combined with CeO₂ synthesized by coprecipitation within reverse microemulsion.
- Stable performance in pure methane.
- Resistance to carbon deposition and suitable for direct methane oxidation.

A R T I C L E I N F O

Article history:

Received 8 August 2013

Received in revised form

8 November 2013

Accepted 5 December 2013

Available online 31 December 2013

Keywords:

SOFC

Anode

MoNi–Ce

Catalyst activity

Electrochemical performance

Direct oxidation of methane

A B S T R A C T

This paper investigates the catalytic activity and the electrochemical performance of bimetallic formulation combining Mo and Ni with CeO₂ (MoNi–Ce) in relation its potential use as anode material for SOFC. The catalytic properties were evaluated for methane partial oxidation as function of temperature and the carbon deposition on the anode surface was analysed by TG-MS. A conversion of 12.8% was reached for partial methane oxidation at 850 °C as well as a high coke resistance. The electrochemical performance was studied in a single cell with La_{0.58}Sr_{0.4}Fe_{0.8}Co_{0.2}O_{3–δ} (LSCF) as cathode, La_{0.9}Sr_{0.1}Ga_{0.8}Mg_{0.2}O_{2.85} (LSGM) as electrolyte and MoNi–Ce as anode. A thin buffer layer of La_{0.4}Ce_{0.6}O_{4–δ} (LCD) between anode and electrolyte was used to avoid possible interfacial reactions. The cell was tested in different humidified fuels (H₂, CH₄ and H₂/CH₄ mixtures) and static air at 750, 800 and 850 °C. The electrochemical behaviour was evaluated by current–voltage curves, impedance spectroscopy and load demand. Stability tests were also performed in pure CH₄ at each studied temperature in order to assess degradation of the electrochemical cell performance. No significant performance degradation was detected in all studied fuels even pure methane, which suggests that MoNi–Ce is a suitable anode material for direct methane SOFC.

© 2013 Elsevier B.V. All rights reserved.

1. Introduction

The development of ceramic anodes for the direct use of hydrocarbon fuels at intermediate temperature is becoming an important challenge in solid oxide fuel cell (SOFC) development. Ni/YSZ cermet is the most commonly used anode material for SOFC technology. Although Ni is an excellent catalyst for the electrochemical oxidation of hydrogen and has good electrical conductivity, it exhibits a poor redox stability, low tolerance to sulphur and carbon deposition when using hydrocarbon fuels and the tendency of nickel agglomeration after prolonged operation [1,2]. Then, many efforts have been made to develop new anode materials for SOFC,

such as doped CeO₂ [3–5], doped LaCrO₃ [6–8] and Sr₂MgMoO_{6–8} based double perovskites [9–11].

Among these materials, CeO₂-based anodes have shown considerable promise for the direct oxidation of CH₄. Doped-ceria materials can be operated at lower temperatures because of their mixed ionic and electronic conductivity under reducing conditions, and also show an ability for continuous carbon cleaning due to oxygen storage/release; as well as a good electrocatalytic activity for oxidation of methane. However, although doped ceria has been predicted to have the ability to oxidize hydrogen and methane, a more reactive anode with higher electronic conductivity is required [5,12,13]. Therefore, introducing transition elements into CeO₂ could provide additional pathways for redox reactions at the anode surface, facilitating its electrocatalytic reaction for oxidation of fuels. In this context, Ni–CeO₂/YSZ anodes showed excellent stability during CH₄ reforming

* Corresponding author.

E-mail address: m.escudero@ciemat.es (M.J. Escudero).

and some tolerance to H_2S contamination [14,15] and doping additional metals in the Ni–YSZ anode such as Mo, Pt, Au and La are beneficial to the reforming reaction of hydrocarbons, due to their functions of breaking the C–H bond more easily. In addition, molybdenum appeared in the composition of promising anode materials for running on hydrocarbons or H_2S as fuels, such as double perovskites based on $\text{Sr}_2\text{MgMoO}_6$ and $\text{Sr}_2\text{CoMoO}_6$ [9,11,16] and mixed metal sulphides M–MoS_2 ($\text{M} = \text{Fe, Co, Ni}$) [17].

Based on these studies, doping with hexavalent Mo to Ni– CeO_2 could improve the catalytic activity of hydrocarbon oxidation and reduce the carbon deposition. In a previous work [18], a bimetallic Mo–Ni formulation combined with CeO_2 , named hereafter MoNi–Ce, was studied in terms of structural properties as SOFC anode material and revealed that this compound exhibited an acceptable electrical conductivity (0.23 S cm^{-1} at 750°C in 10% H_2/N_2) and a thermal expansion coefficient ($13.3 \times 10^{-6} \text{ K}^{-1}$) close to other SOFC cell components. In the present paper, we have investigated the catalytic activity of MoNi–Ce for methane oxidation as function of temperature and its electrochemical performance as alternative SOFC anode in a single cell based on $\text{La}_{0.9}\text{Sr}_{0.1}\text{Ga}_{0.8}\text{Mg}_{0.2}\text{O}_{2.85}$ (LSGM) electrolyte running with hydrogen and/or methane as fuels at 750, 800 and 850°C .

2. Experimental

2.1. Synthesis and characterization of anode material

Mo–Ni combined with CeO_2 (MoNi–Ce) with a total loading of 30 at.% (1/5 atomic ratio for Mo/Ni system) was prepared by coprecipitation within reverse microemulsions using the following salts: cerium (III) nitrate hexahydrate (Fluka, purity >98%), nickel (II) nitrate hexahydrate (Panreac, purity >99%) and ammonium molybdate tetrahydrate (Fluka, purity >99%) as precursors. For this purpose, two reverse microemulsions, of similar characteristics concerning the volumes employed of organic (n-heptane from Panreac), aqueous phases of surfactant (Triton X-100 from Sigma Aldrich) and co-surfactant of (1-hexanol from Sigma Aldrich), were prepared. The first one contained in its aqueous phase the dissolved salts of Ce, Ni and Mo, while the second one contained in its aqueous phase a dissolved base (tetramethyl ammonium hydroxide or TMAH from Sigma Aldrich) which is employed as precipitating agent. Mixing both microemulsions produces the precipitation of the cations and after separation of the precipitated solid by centrifugation and decanting, the resulting solid was rinsed with methanol and dry for 24 h at 150°C . Then, the resulting material is then calcined under air at 800°C during 2 h, employing a heating ramp of 1°C min^{-1} .

The porosity distribution of anode material was measured using an Autopore IV 9500 mercury porosimeter. Before each measurement the sample was outgassed at 80°C for 12 h. X-ray powder diffraction (XRD) patterns were obtained using a PANalytical X'Pert Pro diffractometer, equipped with a $\text{Cu K}\alpha$ (1.5406 \AA) radiation source. The scans were collected in the 2θ range ($4\text{--}90^\circ$) with 0.04° step and 2 s counting time per point. X-ray photoelectron spectra (XPS) were recorded with a Perkin–Elmer PHI 5400 spectrometer equipped with a $\text{Mg K}\alpha$ excitation source ($h\nu = 1253.60 \text{ eV}$) and a beam size of 1 mm diameter. Typical operation conditions were: X-ray gun, 15 kV, 20 mA, pressure in the sample chamber $\sim 10^{-9}$ Torr, pass energy, 89.50 eV for general spectra ($0\text{--}1100 \text{ eV}$) and 35.75 eV for high resolution spectra. In order to take into account the charging effects on the measured binding energies, these energies were determined by referencing to the C 1s peak at 284.8 eV. The chemical analysis of the compound was measured by EDX method using a Hitachi microscope S-2500 combined with EDX, model Sun Sparcstation taking into account of eight measurements at different points of the solid material.

2.2. Catalytic evaluation

Catalytic activity measurements for methane oxidation were tested in a tubular quartz reactor at atmospheric pressure from 400 to 850°C . The catalyst bed was formed by 0.23 g of sample (0.25–0.42 mesh) and an inert diluter (SiC) in a 1/3 v/v. Prior to the catalytic measurements, the calcined sample was reduced *in situ* with 10% H_2/Ar mixture (50 ml min^{-1}) at room temperature up to 850°C and isothermally kept at this temperature for 10 h. To assess the oxidation activity for methane partial oxidation a 5:2 $\text{CH}_4:\text{O}_2$ mixture was used with a total flow rate of 50 ml min^{-1} ($\text{GHSV} = 20,200 \text{ h}^{-1}$). Argon was employed as the balance gas. Reaction products were analysed with a Varian 3400 chromatograph connected in line, equipped with a TCD detector and molecular sieve 13 Å and Porapak Q columns.

At the end of catalytic run, the sample was subjected to a temperature programmed oxidation (TPO) test in order to estimate the carbon deposition. TPO experiment was carried out in 10% O_2/Ar mixture (50 ml min^{-1}) from room temperature up to 1000°C with a rate of $10^\circ\text{C min}^{-1}$ using a Mettler Toledo TGA/SDTA 851e thermobalance. Gases evolution was analysed with a Pfeiffer Omnistar quadrupole mass spectrometer.

2.3. Single cell fabrication and test

A single cell was fabricated with an active area of 0.28 cm^2 , and supported by $\text{La}_{0.9}\text{Sr}_{0.1}\text{Ga}_{0.8}\text{Mg}_{0.2}\text{O}_{2.85}$ (LSGM) electrolyte from Praxair. The electrolyte pellet was prepared by uniaxial pressure and calcination at 1500°C for 10 h from the powder electrolyte. The surface of the electrolyte was roughened by mechanical grinding to reduce its thickness. After sintering, a dense LSGM pellet was obtained with a diameter of $\sim 11 \text{ mm}$ and a thickness of $\sim 0.4 \text{ mm}$. Subsequently, a porous $\text{La}_{0.4}\text{Ce}_{0.6}\text{O}_{4-\delta}$ (LCD, Praxair) layer was deposited onto one side of the dense electrolyte by tape casting using PMMA as pore former and then annealing in air at 1400°C for 2 h. The thin buffer layer of LDC was placed between the electrolyte and anode, in order to prevent formation of unwanted phases at the anode electrolyte interface due to the possible reaction of Ni and LSGM under reducing conditions at high temperature [19]. Then, MoNi–Ce powder was mixed with desired amount of Decoflux (WB41, Zschimmer and Schwartz) binder to obtain a slurry that was applied onto the LCD deposited by screen-printing and heated at 850°C for 2 h. The cathode ink was prepared by de-agglomerating the $\text{La}_{0.58}\text{Sr}_{0.4}\text{Fe}_{0.8}\text{Co}_{0.2}\text{O}_{3-\delta}$ (LSCF, Praxair) powder using rotatory ball milling in acetone with 2 wt.% of Hypermer KD1 dispersant (TWC). After this step, the agglomerated slurry was added to an ink vehicle consisting of 5 wt.% polyvinyl butyral, PVB (Butvar, Sigma–Aldrich) in α -terpineol (Fluka). This mixture was stirred until the acetone had fully evaporated. This cathodic ink was deposited by screen-printing onto the other side of dense electrolyte, and then calcined at 850°C for 2 h. Platinum and gold, pastes and wires, were used as current collector for cathode and anode respectively and fired at 850°C 1 h. Finally, cell was attached to an alumina tube with a ceramic seal (Aremco, Ceramabond 552) and placed into a furnace.

Humidified hydrogen and/or methane were supplied to the anode as fuel at a flow rate of 50 ml min^{-1} after passing through a saturator at room temperature to adjust the gas humidity at 3% H_2O . Cathode was open to air.

Electrochemical measurements were conducted using AUTOLAB system (PGSTAT30 and FRA2 module) from Eco Chemie. The current voltage (I – V) characteristic of the cell was measured using linear sweep voltammetry at a scan rate of 10 mV s^{-1} . The impedance of the cell was recorded at open circuit in galvanostatic mode in a frequency range from 1 MHz to 10 mHz and excitation signal of 5 mA.

3. Results and discussion

3.1. Anode material characterisation

The pore-size distribution curve of MoNi–Ce, studied by Hg-porosimetry, is presented in Fig. 1. The sample possess porous structure with a size distribution of 5–15 nm and the average pore diameter is 10.1 nm, but most pores lie in near 7.5 nm.

Fig. 2 shows the XRD patterns of MoNi–Ce before and after its reduction in 10% H₂ for 24 h at 800 °C. Initially, the compound mainly exhibits a phase of cubic fluorite type structure of CeO₂ and a second cubic phase of NiO. No characteristics peaks of molybdenum oxides were observed. This could be interpreted as it took place the substitution of Mo⁶⁺ for Ce⁴⁺ in fluorite phase, producing an anion (oxygen) excess in its interstitial position. The possible introduction of dopant into the fluorite lattice is corroborated by the variation on the lattice parameter. The comparison of XRD patterns for pure CeO₂ and that for monometallic Ni–Ce sample (30 at.% Ni–CeO₂), both of them synthesized by microemulsion method and calcined in air at 800 °C, revealed a decrease in the lattice parameter, $a = 0.5410$ nm and 0.5393 nm, respectively. This decrease is consistent, considering the ionic radius (Ce⁴⁺: 0.97 Å; Ni²⁺: 0.69 Å; Mo⁶⁺: 0.42 Å), with the partial substitution of Ni²⁺ for Ce⁴⁺ in CeO₂ structure. In the case of bimetallic MoNi–Ce sample (30 at.% total metal load, Mo/Ni 1/5) the lattice parameter (a) was 0.5396 nm, lower than that obtained for pure ceria but very similar to the analogous monometallic sample (Ni–Ce). The slight difference between the lattice parameter of Ni–Ce and MoNi–Ce does not give enough evidence to assert the incorporation of Mo⁶⁺ into the fluorite lattice. Notice that Mo content in MoNi–Ce sample is very low and expected variations might be practically indistinguishable.

After its reduction, the compound kept the reflections assigned to fluorite structure and also appeared peaks ascribed to metal Ni with cubic structure. No sign of Ce₂O₃ phase was detected, so this is indicated that cerium is present mainly in the form of Ce⁴⁺.

XPS was used to study the chemical state of the elements. The Ce 3d, Mo 3d and Ni 2p signals of MoNi–Ce before and after its reduction are illustrated in Fig. 3. According to the thoroughly accepted convention suggested by Burroughs et al. [20], in which vⁿ and uⁿ refer to 3d_{5/2} and 3d_{3/2} spin-orbit component of cerium ion, respectively. In the case of pure CeO₂, v, v^{II} and v^{III} peaks for the Ce 3d_{5/2} core level and u, u^{II} and u^{III} peaks for the Ce 3d_{3/2} core level can be identified in its XPS spectrum. For pure Ce₂O₃, v₀ and v^I features for the Ce 3d_{5/2} core level and u₀ and u^I features for the Ce

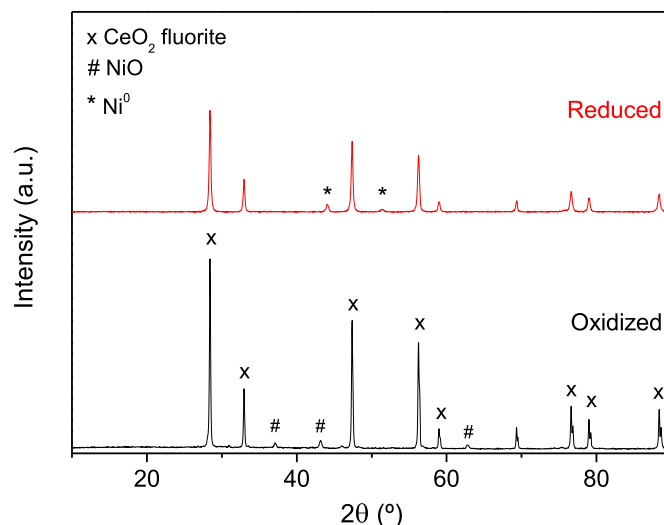


Fig. 2. XRD patterns of MoNi–Ce before and after reduction in 10% H₂ for 24 h at 800 °C.

3d_{3/2} core level can be appreciated [21]. In air, the Ce spectrum contained three main 3d_{5/2} peaks at 882.4 (v), 888.9 (v^{II}) and 898.3 (v^{III}) eV, and two main 3d_{3/2} signals at 901.0 (u) and 907.8 (u^{II}) eV. According to literature, these peaks are attributed to Ce⁴⁺ [21]. It is worth mentioning that only 5 peaks of Ce 3d can be appreciated in Fig. 3a, the reflection corresponds to u^{III} of the 3d_{3/2} core level at 916.0 eV was not recorded. After its reduction, the spectrum showed similar profile but the intensity of signals is weaker than that of the oxidized one. In addition, it can be observed significant peaks located at binding energy 882.4 and 898.6 eV for 3d_{5/2} and 901.0 eV for 3d_{3/2}, indicating the presence of Ce⁴⁺. No signals typical of Ce³⁺ at 886.2 and 904.7 eV were observed [22]. However, it is noted that the satellite signals of v^{II} and u^{II} for the 3d_{5/2} and 3d_{3/2} levels respectively, cannot be distinguished or show very weak reflections. This could indicate a slight reduction of Ce⁴⁺. The aforementioned XPS results were in good agreement with the XRD results, and implied that the cerium is mainly as Ce⁴⁺ in oxidized and reduced samples.

The Mo 3d spectra of the oxidized Mo–Ce shows two peaks located at 232.1 and 235.3 eV that correspond to the doublets Mo 3d_{5/2} and Mo 3d_{3/2}, respectively (Fig. 3b). These binding energy values are attributed to Mo⁶⁺ [23]. After its reduction, the profile of Mo 3d level is shifted towards low binding energies, and presents three signals at 228.0, 232.3 and 235.5 eV. The de-convoluted peaks (not shown) revealed four doublets located at 228.0 and 231.1 eV, 229.0 and 232.0 eV, 230.4 and 233.5 eV, 232.3 and 235.5 eV and they have assigned to Mo 3d_{5/2} and Mo 3d_{3/2} peaks of Mo⁰, Mo⁴⁺, Mo⁵⁺ and Mo⁶⁺ states, respectively [24]. These results confirmed that the physical state of molybdenum is hexavalent (Mo⁶⁺) in the oxidized sample, whereas after reduction lower valences states, Mo⁵⁺, Mo⁴⁺ and Mo⁰, coexist with Mo⁶⁺.

From the Ni 2p spectra (Fig. 3c), the oxidized component shows a main peak Ni 2p_{3/2} at 854.7 eV with a shape-up satellite at 861.1 eV that is characteristic of NiO [25]. However, notable changes were observed in the reduced sample that presents two weak peaks at 852.6 and 856.2 eV with a satellite at 862.3 eV. According the literature, these peaks correspond to metallic nickel and Ni²⁺ in NiO and Ni–Mo alloy, respectively [26,27].

EDX microanalyses were performed on eight surface points of compound and revealed that the average atomic concentrations are 25 at.% of Ni, 5 at.% of Mo and 70 at.% of Ce for both oxidized and reduced samples. This indicates that molybdenum is not lost in the reduction process.

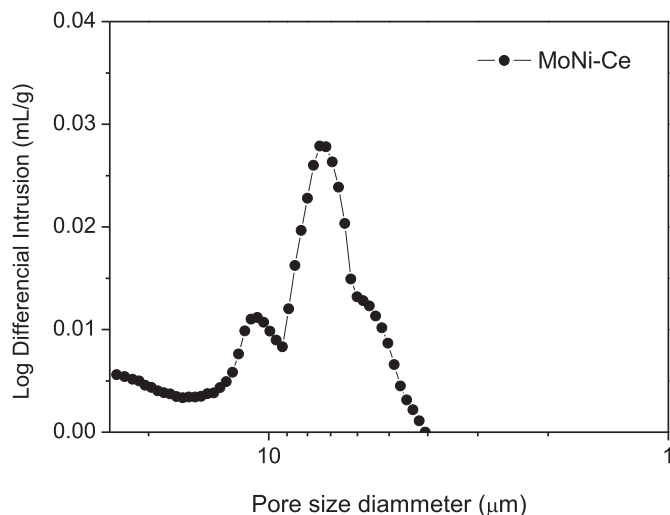
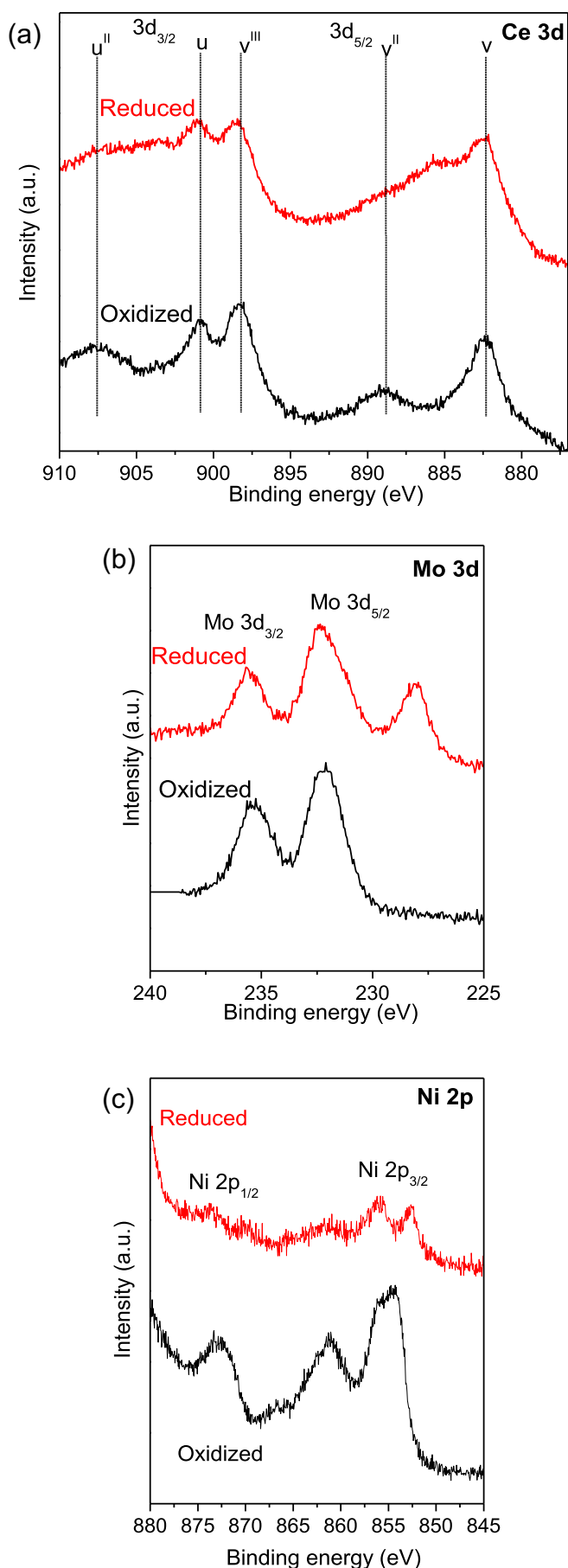


Fig. 1. Pore size distribution curve for MoNi–Ce.



3.2. Catalytic activity measurements

In the SOFC anode operating environment, oxygen is transported from the cathode to the anode under polarization. Although passing gas mixture over a catalytic bed does not exactly replicate the anodic condition but it is perhaps the best approximation than can be achieved. The catalytic capability of MoNi–Ce sample for partial methane oxidation was investigated as function of temperature, from 400 to 850 °C. Previous to the catalytic activity tests, different residence times as well as stoichiometries of gas mixture were tested to select the conditions to perform the methane oxidation using MoNi–Ce as catalyst. The selected conditions were as follow: W/F (catalyst weight/feed fuel flow rate) = 8 g h mol⁻¹, total flow rate = 50 ml min⁻¹ and 5:2 CH₄:O₂ gas stream composition. Blank test was carried out filling the reactor only by SiC to avoid hot spots under the same experimental conditions. No reactions were detected in the gas phase below 700 °C, whereas a methane conversion of 6.7% was achieved at 850 °C. Blank test results are included in Fig. 4, together with that for the steady state curve obtained by 5:2 CH₄:O₂ gas mixture on sample. The reaction starts above 700 °C for MoNi–Ce and the oxidation products are CO₂, H₂, CO and H₂O. These results evidence that several reactions take place on the catalyst surface. Methane conversion increased with the temperature and reached 12.8% at 850 °C.

Besides a good activity for methane conversion, the anode catalyst should also display a high resistivity towards carbon deposition. The formation of carbon over the anode may destruct the integrity of the anode layer, the methane would contact the anode directly and results in the carbon deposition over the anode layer which could occupy the active sites to cause a rapid irreversible cell deterioration [28]. After cooling the reactor, to investigate the possible carbon formation, temperature programmed oxidation (TPO) studies were conducted at the end of catalytic reactions. The TGA analysis of MoNi–Ce sample in oxygen after the catalytic test is shown in Fig. 5a. The initial slight weight loss of 0.02% below 150 °C may be attributed to the desorption of surface-adsorbed water. The slight weight gain near 300 °C is due to the oxidation of nickel on reduced MoNi–Ce sample. After that, a significant weight decrease, centred at 340 °C, is observed and associated to the oxidation of carbon to form CO₂. The TPO profile with the CO₂ ($m/z = 44$) signal is illustrated in Fig. 5b. This analysis (Fig. 5b) revealed very low carbon coverage on post-reaction sample (<0.04 wt.%). It can be observed only one unique peak of CO₂ around 340 °C what evidences the reoxidation and carbon removal observed in TGA. This low temperature indicates that the carbon deposits could be easily removed on MoNi–Ce surface in SOFC operating conditions. According to bibliography, the nature of the carbonaceous deposits that appear below 400 °C could be associated to carbon species well dispersed (atomically) over the metallic particles [29,30]. A small shoulder is observed at temperatures above 600 °C that corresponds to the molybdenum oxidation on reduced MoNi–Ce sample. Finally, at higher temperatures (>750 °C), a new weight gain is detected due to the reoxidation of doped ceria.

3.3. Performance in single cell

Methane is the major compound of natural gas and can be used as fuel for SOFC. Gas mixtures consisting of methane, hydrogen and water correspond to the situation of no external reforming of methane and different pre-reforming situations. The MoNi–Ce

Fig. 3. XPS spectra of Mo–Ce before and after its reduction in 10% H₂ at 800 °C for 24 h: a) Ce 3d core level region; b) Mo 3d core level region; c) Ni 2p core level region.

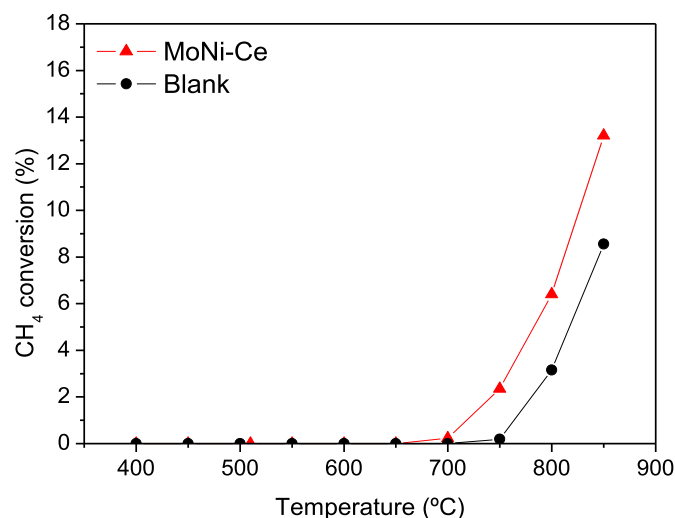


Fig. 4. Catalytic activity of MoNi-Ce for condition of partial methane oxidation (5:2 CH₄:O₂). (Br) represents the blank reactor.

compound was tested as the anode material in a single cell running on wet H₂, CH₄ and mixtures H₂/CH₄ as fuels at 750, 800 and 850 °C and static air as oxidant to evaluate its electrochemical performance. The testing cell was assembled with a ~400 μm thick LSGM electrolyte, a porous LSCF cathode and a thin LCD buffer layer between the electrolyte and the anode (MoNi-Ce/LDC/LSGM/LSCF single cell). The LSCF cathode exhibits the desired crystalline phase

(rhombohedral perovskite structure) at the calcination temperature of 850 °C. The phases were relatively pure because there was no observable evidence of impurity or secondary phases. The particle size, obtained from XRD analysis, was 0.025 μm. The porosity of sintered cathode was determined by mercury porosimetry and was 75.8% whereas the average pore diameter was calculated to be 10.9 nm.

The open circuit voltage (OCV) of the cell was recorded at different wet H₂/CH₄ mixtures at 750, 800 and 850 °C as shown in Fig. 6. Except from pure methane at 750 and 800 °C, the representing values correspond to equilibrium conditions measured during 1 h. Note that at 750 and 800 °C in pure CH₄, the OCV value decreased gradually with the time indicating that the operation of methane is not stable at open circuit. This could be due to the carbon deposition on the anode.

In wet pure hydrogen, the OCV decreases from 1.04 to 1.02 V with increasing temperature in the range 750–850 °C, while the OCV in pure CH₄ increases (0.85–1.02 V). Both trends with temperature agreed with calculated OCV based on the thermodynamic equilibrium in wet (3% H₂O) H₂ and CH₄ [7]. However, the theoretical values in both atmospheres are higher than that measured on the cell. Similar behaviour was also observed in cells with interfaces of LSGM/LDC by Guo [31] and Li [32]. They suggested that the lower OCV values are not caused by gas leakage across the electrolyte, based on the facts of dense electrolyte, low measured gas leakage rate and stable OCV value with changing gas flow rate. The low OCV can alternatively be explained by the diffusion of transition metal cations (e.g. Co, Fe, Ni and Mo) from electrodes into LSGM layer during sintering [32–34]. The diffusion of transition metal cations from electrodes to LSGM electrolyte could yield an electronic conduction. Then, the electrolyte is not a pure ionic conductor due to a residual electronic conductivity, and the OCV could be estimated as a mixed conductor as follows:

$$OCV = t_i \frac{RT}{4F} \ln \frac{P_{O_2(C)}}{P_{O_2(A)}} \quad (1)$$

where t_i is the average ionic transference number [$\sigma_{ionic}/(\sigma_{ionic} + \sigma_{electronic})$], R is the gas constant, T the temperature, F the Faraday constant, and P_{O_2} the partial oxygen pressure at the electrode (cathode and anode).

In addition, the use of static air as oxidant instead of an oxygen flow could also affect to the decrease of the OCV value.

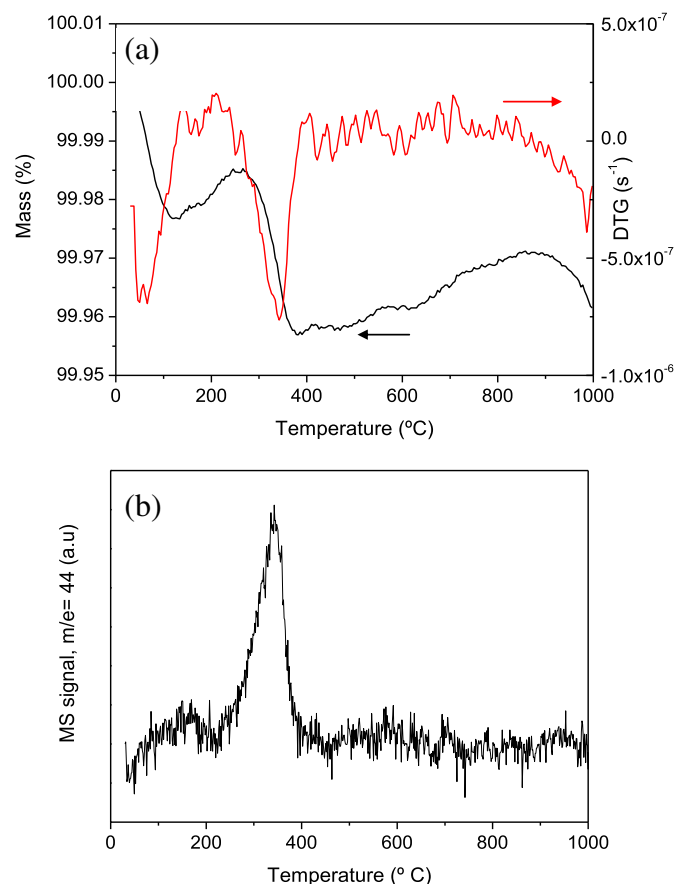


Fig. 5. TPO test performed over MoNi-Ce sample after catalytic test in 10% O₂/Ar from 30 to 1000 °C at 10 °C min⁻¹: (a) TGA analysis; (b) Evolution of CO₂.

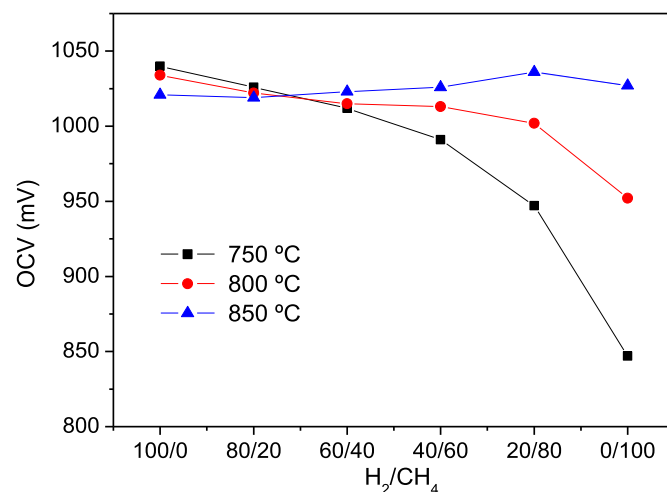
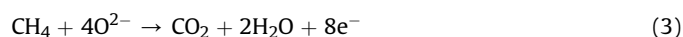


Fig. 6. Open circuit voltages (OCV) of the MoNi-Ce/LDC/LSGM/LSCF cell collected in various wet H₂/CH₄ fuel ratios at different temperatures.

On the other hand, the effect of varying CH₄ concentration in H₂ on OCV changes depending on the operation temperature. At 750 and 800 °C, the increase of CH₄ concentration, with decreasing of H₂ in the fuel composition, reduces the OCV value being most significant at 750 °C. This could be associated with a reduced H₂ partial pressure on the anode. In the case of 850 °C, it is worth nothing that the OCV values show a slight increase. When the CH₄ content in the feeding gas is higher than 20%, the OCV data increase with increasing temperature as well as the difference among their values is more considerable at high CH₄ concentration.

It is well known that information about anode reactions can be obtained from OCV measurements but, unfortunately, the OCV interpretation under methane is always more complicated because the likelihood of alternative routes for methane oxidation [5,35–37]. Possible mechanism for the oxidation of methane in humidified atmospheres can be: steam reforming (2), direct oxidation (3) or partial oxidation (4); once carbon dioxide, carbon monoxide, hydrogen and steam have been produced then further reactions (5 and 6) and can occur in addition to water gas shift (7), cracking (8) and Boudouard reaction (9):



From the above reactions, it is possible that the different OCVs observed are due to the contribution of each reaction in different proportions. Furthermore, the extent of contribution of each reaction depends solely on the catalytic properties of the anode material which in turn is temperature dependent. Thus, if the process involves hydrogen production, e.g. via methane reforming (Reaction (2)) or via methane cracking (Reaction (8)) the OCV decreases with increasing temperature, which is in clear disagreement with our data. Then, one may assume that the mechanism involves oxidation could be direct methane oxidation (Reaction (3)) or partial methane oxidation (Reaction (4)). However, the observed increase of OCV with the operating temperature when methane is used as fuel suggests in this sense a predominance of partial electrochemical oxidation in the process [35]. Therefore, these results suggest that the methane oxidation on MoNi–Ce surface may occur in multiple steps, so that the equilibrium is established between the methane and partial oxidation products which are influenced by temperature.

A selection of the voltage and power density curves as function of current density for the cell in different wet fuel atmospheres at 750, 800 and 850 °C are presented in Fig. 7. It can be seen that the maximum current density (cell voltage = 0 V) and the power density decrease with increasing the CH₄ content and decreasing of temperature. The maximum power densities for the cell were 298, 443 and 589 mW cm^{−2} in H₂ and 85, 182 and 358 mW cm^{−2} in CH₄ at 750, 800 and 850 °C, respectively, as well as the maximum current densities were of 1241, 1822 and 2358 mA in H₂ and 290, 730 and 1338 mA in CH₄ at the above mentioned temperatures.

Table 1 summarizes the results of maximum current densities and maximum power densities obtained in different H₂/CH₄ mixtures at various temperatures. The decrease in cell power density and the maximum current density for the increase of methane content and decreasing of hydrogen may be related to the higher mass of methane molecules, which yields lower gas-phase diffusion and increased concentration polarization. However, it is also noted that each methane molecule reacts with four times as many oxygen ions as each hydrogen molecule, so less methane gas-phase diffusion is needed to yield the same cell current density. Another possible explanation is a difference in the nature of the oxidizing and reducing species, which makes the charge transfer in methane more complex and difficult. H₂ is obviously more active and more effective for reduction. CH₄ is much less reactive than H₂ in heterogeneous oxidation, thus resulting in a higher polarization resistance associated with slower electrochemical oxidation of methane versus hydrogen [38].

Impedance spectroscopy (IS) was also used to study the effect of the presence of methane in the feeding gas and the temperature on the cell performance. Impedance spectra were measured at OCV using a two-probe in H₂, CH₄ and various H₂ and CH₄ mixtures at 750, 800 and 850 °C, they are represented in Fig. 8. The inductive impedance responses were subtracted from the spectra, because it is a well-known fact that they were caused by the measurement devices and connected wires [39]. Each impedance spectra appeared in form of depressed arcs that were larger with the decrease of temperature and the increase of CH₄ content in the feeding gas.

All obtained impedance data for the cell showed in Fig. 8 were fitting by the Zview software (Scriber Associates) to the equivalent circuit $R_s(RQ)_1(RQ)_2(RQ)_3$. No strict physical meaning was given a priori to any circuit elements. In this notation, R is a resistance, and Q a constant phase element with the admittance $Y^* = Y_0(j\omega)^n$, where Y_0 is an admittance scaling factor, j the imaginary unit, ω the angular frequency, and n the frequency exponent. R_s is the ohmic resistance of cell (mainly associated with the electrolyte); each of the (RQ) subcircuits describes a limiting process contributing an impedance arc. The capacitance and relaxation frequency of each contribution can be calculated according to Eqs. (10) and (11) respectively [40].

$$C = (R^{1-n}Q)^{1/n} \quad (10)$$

$$\omega_i = (RQ)^{-1/ni} \quad (11)$$

The relaxation frequency is a very useful tool to identify the processes. The polarization resistance (R_p) of the cell is determined as the sum of the resistances of each individual process ($R_p = R_1 + R_2 + R_3$) and includes reaction and transport resistances from both the anode and the cathode.

The non-ohmic part of the impedance reveals three distinct rate limiting process. The processes have relaxation frequencies at high 15,000–33,000 Hz, 2–9 Hz and 0.1–0.05 Hz. Table 2 gives the resistance values obtained from fitting to the IS data at different temperatures and fuels. Good fitting between the equivalent circuit and the experimental was observed. The impedance data are clearly separated at high, medium and low frequencies designated as (R_1Q_1) , (R_2Q_2) and (R_3Q_3) , respectively. Note that both the ohmic resistance (R_s) and the resistance (R_1) associated at the arc at high frequency are affected by the temperature and are independent of the fuel composition. In addition, the resistance (R_3) attributed at low frequency shows a large dependency on both the operation temperature and methane content, so R_3 notably increases with increasing methane concentration and decreasing temperature.

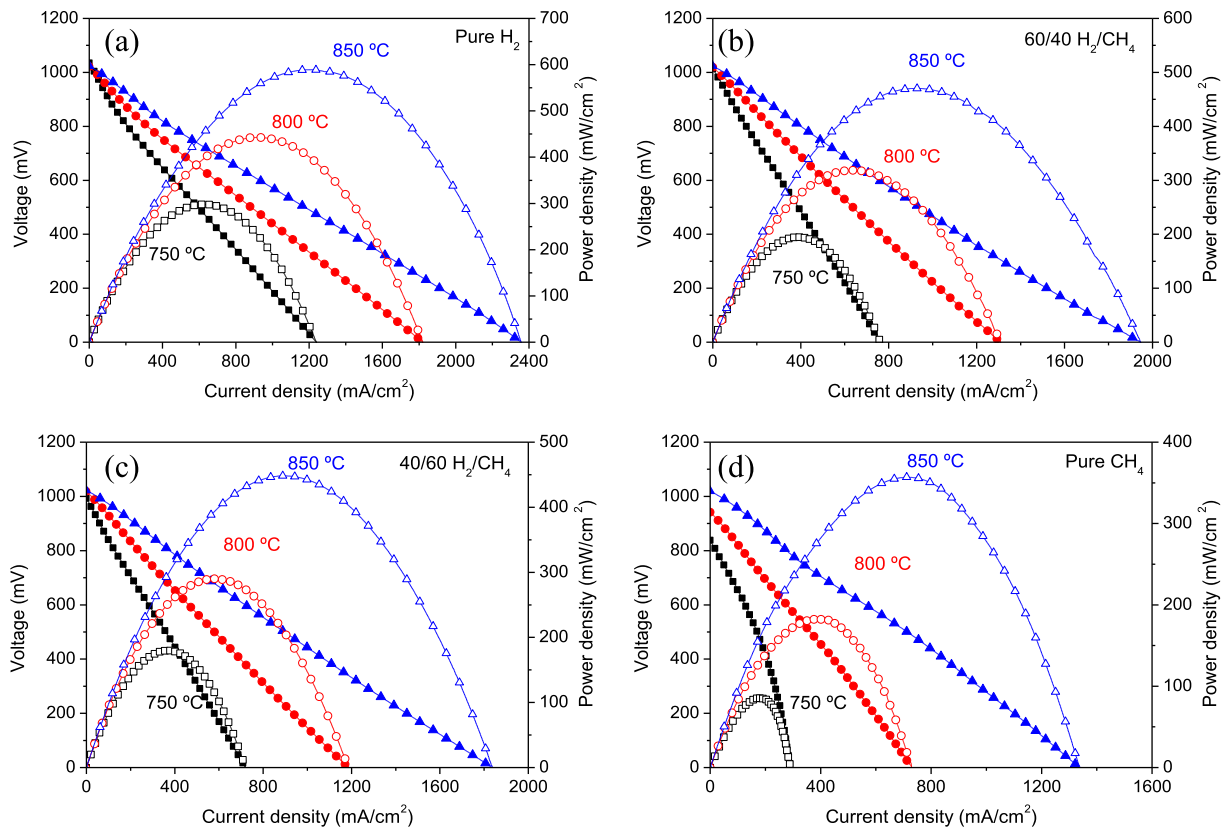


Fig. 7. Voltage and power density versus current density for the MoNi–Ce/LDC/LSGM/LSCF cell in various wet H_2/CH_4 fuel ratios and static air at different temperatures: (a) pure H_2 ; (b) 60/40 H_2/CH_4 ; (c) 40/60 H_2/CH_4 ; (d) pure CH_4 .

While R_2 assigned to the arc at medium frequency, revealed a reduction with increasing the temperature but no trend can be assigned by fuel composition.

On the other hand, the capacitances for the three arcs are independent of the atmosphere composition. While C_1 and C_3 show a slight increase with increasing the temperature, C_2 remains essentially unchanged. The values of C_1 , C_2 and C_3 are in the range of $0.3\text{--}5 \cdot 10^{-4} \text{ F cm}^{-2}$, $1\text{--}3 \cdot 10^{-1} \text{ F cm}^{-2}$ and $1.8\text{--}46 \text{ F cm}^{-2}$, respectively.

The capacitance associated to high frequency arc is the same order the magnitude of electrochemical reactions [41–43]. In addition, the arc 1 is thermally activated and seems to be independent of gas composition. Then, the high frequency process could be related to the electrochemical charge transfer at the triple phase boundary.

The medium arc has a capacitance of $1\text{--}3 \cdot 10^{-1} \text{ F cm}^{-2}$ and is thermally activated. This high capacitance value could more likely be explained by the adsorption of reactant species on the electrodes (anode and cathode) [39,44,45]. However, this process is not affected by fuel composition. So, the medium frequency arc could be related to adsorption or dissociation of adsorbed oxygen in the cathode which is favoured at lower temperatures.

Therefore, specially the low arc frequency appeared to arise entirely from the anode. The capacitance values associated to this arc (low frequency) are very larger ($1.8\text{--}46 \text{ F cm}^{-2}$) and essentially dependent of fuel composition and decrease with increasing temperature. In the present work, MoNi–Ce is a mixed ionic conductor and can change of oxygen nonstoichiometric when the electrode potential is varied and the oxygen incorporation/release reaction at the electrode would also give to a large chemical capacitance [45]. Then, the arc at low frequency could be associated with oxygen exchange reaction and/or diffusion reactions on the anode

electrode and possible chemical reactions (non-charge processes). Capacitances of these magnitudes were also observed by Chen et al. [46] in Ni–SDC anodes under H_2 related to the low frequency arc. They suggested that the large capacitance is associated to the dissociation/diffusion processes of hydrogen on the surface Ni that is promoted by oxygen species such as oxygen vacancies. Jiang et al. [7] investigated the electrocatalytic activity of $(\text{La}_{0.75}\text{Sr}_{0.25})(\text{Cr}_{0.3}\text{Mn}_{0.5})\text{O}_3/\text{YSZ}$ composites for the methane oxidation using three separable arcs and also associated the low frequency arc (0.025 Hz at 900 °C) to the non-charge processes.

Table 1

Maximum current densities and maximum power densities of the MoNi–Ce/LDC/LSGM/LSCF cell in several gas compositions at different temperatures.

Gas composition H_2/CH_4	Temperature (°C)	Maximum current density (mA cm^{-2})	Maximum power density (mW cm^{-2})
100/0	750	1241	298
	800	1822	443
	850	2358	589
80/20	750	805	205
	800	1406	343
	850	2090	508
60/40	750	762	194
	800	1310	319
	850	1948	470
40/60	750	720	180
	800	1187	290
	850	1839	448
20/80	750	685	167
	800	1015	256
	850	1678	424
0/100	750	290	85
	800	739	182
	850	1338	358

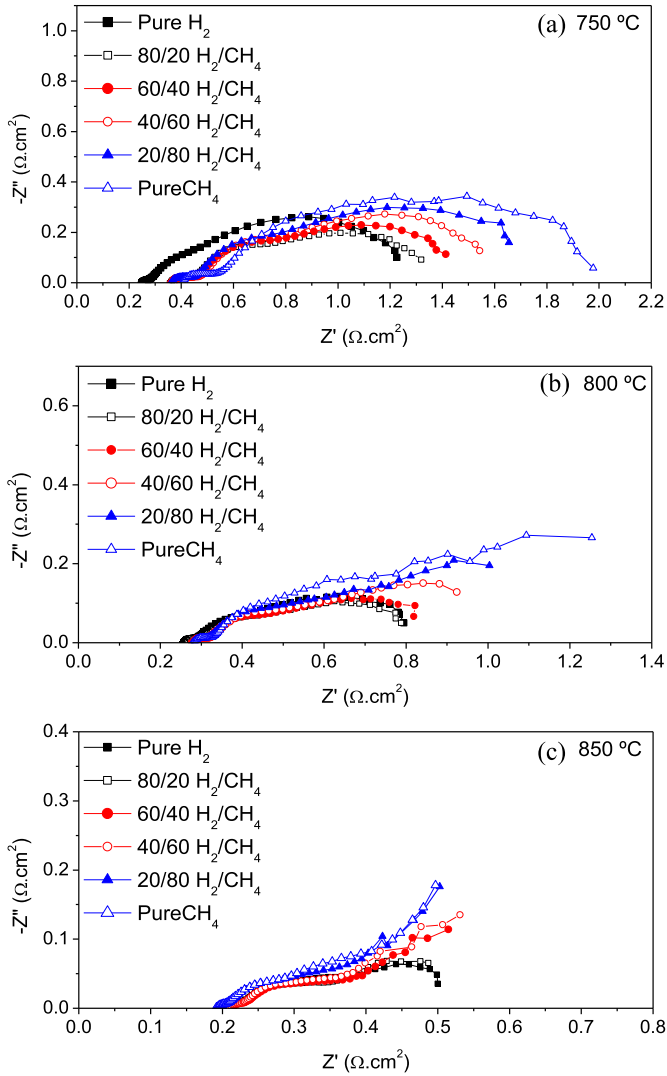


Fig. 8. Impedance spectra for MoNi–Ce/LDC/LSGM/LSCF cell in various wet H_2/CH_4 fuel ratios and static air at different temperatures: (a) 750 °C; (b) 800 °C; (c) 850 °C.

Table 2

Resistance values obtained from the impedance data fitting to equivalent circuit at different temperatures and fuel compositions.

Gas composition H_2/CH_4	Temperature (°C)	R_s ($\Omega \text{ cm}^2$)	R_1 ($\Omega \text{ cm}^2$)	R_2 ($\Omega \text{ cm}^2$)	R_3 ($\Omega \text{ cm}^2$)	R_p ($\Omega \text{ cm}^2$)
100/0	750	0.33	0.12	0.32	0.63	1.07
	800	0.24	0.05	0.14	0.42	0.61
	850	0.20	0.02	0.18	0.14	0.34
80/20	750	0.36	0.15	0.32	0.73	1.20
	800	0.25	0.06	0.16	0.38	0.60
	850	0.19	0.02	0.17	0.17	0.36
60/40	750	0.36	0.16	0.32	0.83	1.31
	800	0.26	0.06	0.15	0.44	0.65
	850	0.20	0.02	0.17	0.24	0.43
40/60	750	0.37	0.17	0.32	0.98	1.47
	800	0.27	0.05	0.18	0.69	0.92
	850	0.20	0.02	0.18	0.58	0.78
20/80	750	0.35	0.16	0.32	1.13	1.61
	800	0.26	0.05	0.18	1.15	1.38
	850	0.19	0.02	0.18	0.72	0.92
0/100	750	0.35	0.17	0.34	1.26	1.77
	800	0.26	0.06	0.20	1.00	1.26
	850	0.19	0.02	0.06	0.40	0.48

Except in H_2 and 80/20 H_2/CH_4 at 850 °C, the low frequency resistance, R_3 , is the main constituent of polarization resistance and this contribution is more notably at lower temperature and the methane content increases. This could indicate that the electro-catalytic activity of MoNi–Ce for fuel oxidation is likely limited by the non-charge processes (oxygen exchange reaction and/or diffusion reactions and possible chemical reaction).

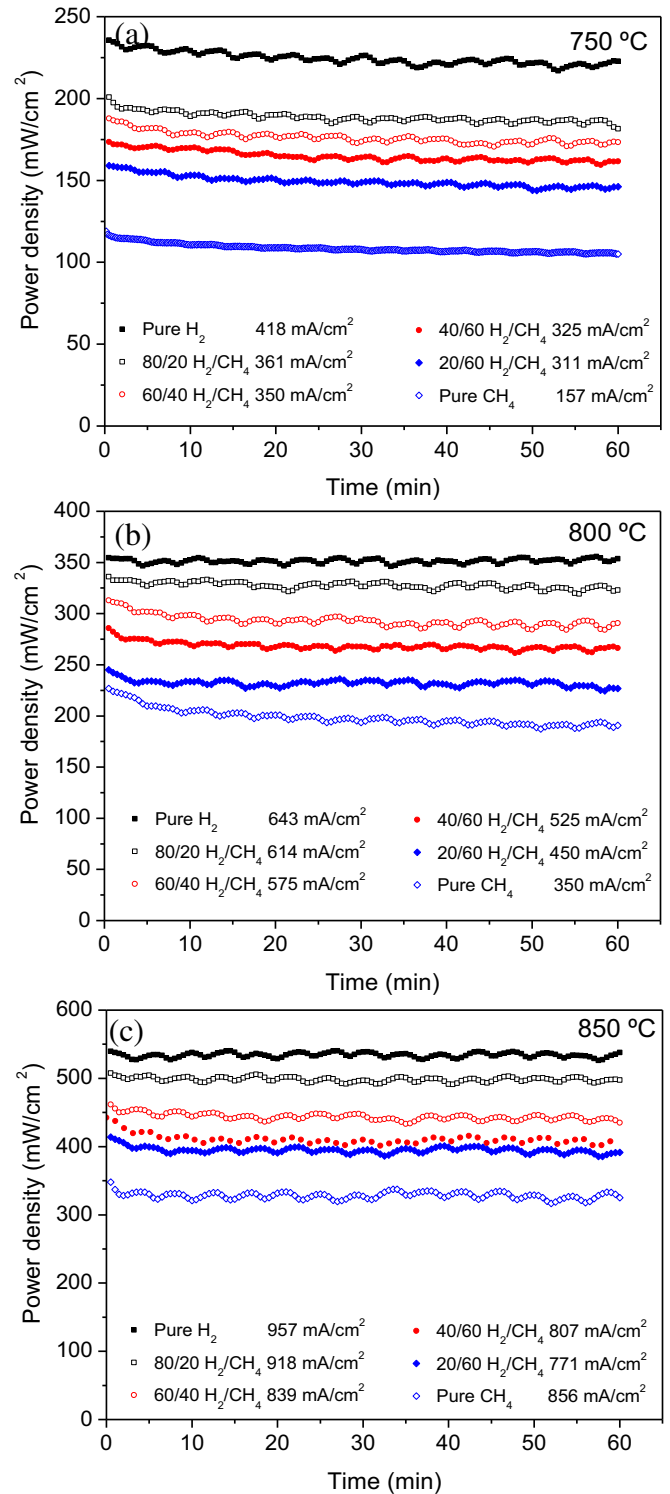


Fig. 9. Power density of the MoNi–Ce/LDC/LSGM/LSCF cell as a function of the operating time in various wet H_2/CH_4 fuel ratios and static air at different temperatures: (a) 750 °C; (b) 800 °C; (c) 850 °C.

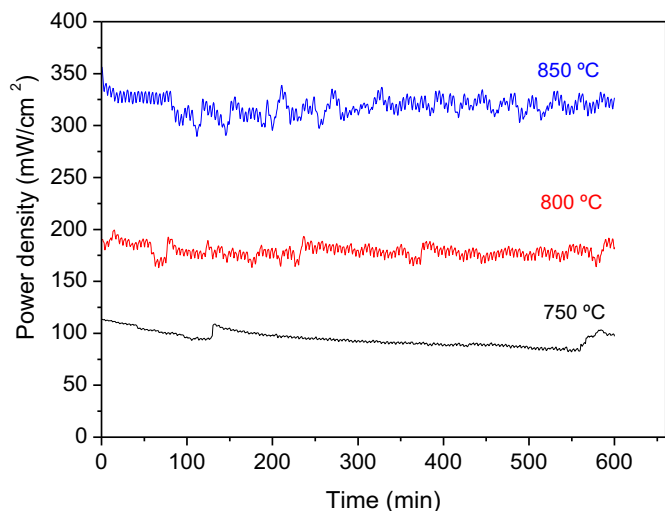


Fig. 10. Endurance test of the MoNi–Ce/LDC/LSGM/LSCF cell in wet CH₄ fuel and static air at 750, 800 and 850 °C.

To investigate the stability of the MoNi–Ce anode material, the cell performance was measured under a constant current for 1 h in each studied gas composition at 750, 800, and 850 °C (Fig. 9). The current density demand varied in each test and corresponded to the intensity required to achieve 90% of the maximum power. Each value was obtained of IV curves measurements in identical experimental conditions before the stability test. Note that the cell was stable in all experimental conditions measured even in pure CH₄. As it was expected, the power density increases with an increase of temperature and a decrease of CH₄ content in the feeding gas. Then,

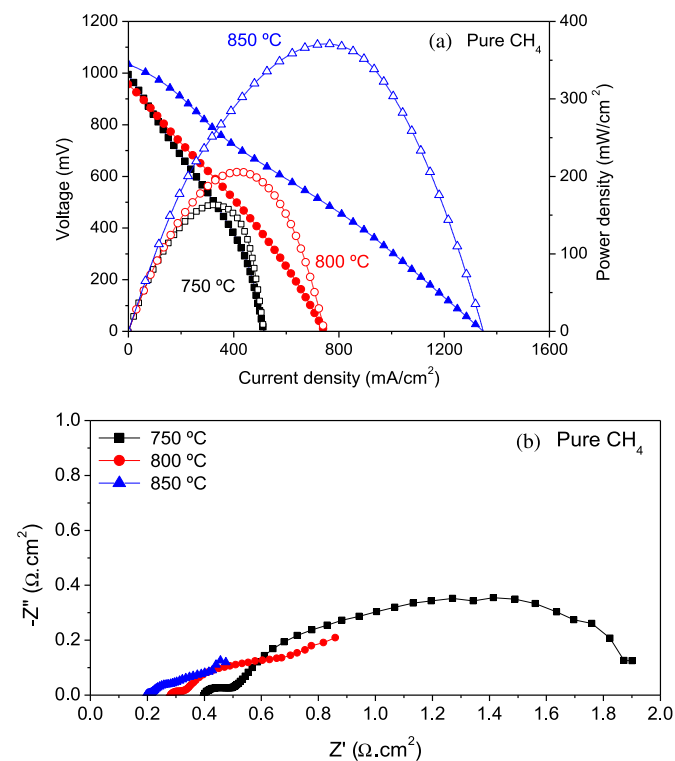


Fig. 11. Electrochemical characterization of the MoNi–Ce/LDC/LSGM/LSCF cell after durability tests for 10 h in wet CH₄ fuel and static air at 750, 800 and 850 °C. (a) IV curves; (b) impedance spectra.

the cell reached power densities of about 222, 355 and 533 mW cm^{−2} in H₂ and 106, 195 and 333 mW cm^{−2} in CH₄ at 750, 800 and 850 °C, respectively. At high temperatures, the benefits of increased catalytic activity at the anode, increased ion transport rates and increased electrochemical activity on both electrodes what allows to reach higher power densities. On the other hand, the presence of CH₄ in the fuel yields a reduction in the H₂ partial pressure that decreases the power density, but can also occur simultaneously the direct oxidation of methane on the anode surface which could diminish this drop. At high current densities, the oxygen species might mostly be used for the direct oxidation of CH₄, CO and H₂, Reactions (3), (5) and (6) above mentioned. Similar IV curves and impedance spectra were measured before and after the stability tests.

Finally, long-term tests were performed in order to evaluate the resistance to carbon deposition (Fig. 10). Based on thermodynamic predictions of the equilibrium reaction products for direct methane operation, high current densities are required to avoid coking and maintain a stable operation [47,48]. As the current increased the amount of O^{2−} transported from cathode to anode increased and the amount of H₂O began to increase. When CH₄ is used as fuel, the presence of oxygen anions produces the species CO, CO₂, and H₂O in addition to H₂ and C. At low current densities, C and H₂ are species predominant (Reaction (8)). As the current density increases, the solid carbon is replaced by CO that is produced by the endothermic steam reforming reaction (Reaction (2)) and/or the partial oxidation of methane (Reaction (4)). The production of CO may also be a result of the oxidation of carbon deposits and/or the reaction of water with carbon. At high operating current densities, solid carbon is not thermodynamically predicted and the CO₂ and H₂O concentrations increase. CO₂ may be produced by the direct electrochemical oxidation of methane (Reaction (3)), and/or the exothermic water gas shift reaction (Reaction (7)). Then, the cell was tested in pure CH₄ for 10 h at constant current density of 157, 356 and 654 mA cm^{−2} at 750, 800 and 850 °C, respectively as shown in Fig. 10. These values correspond to about 90% of current density at maximum power. The cell performance remained stable in these time periods indicating no significant carbon deposition on the anode surface. As mentioned before, at high current density the major production of oxygen species allows simultaneously the hydrogen oxidation and the carbon monoxide oxidation to carbon dioxide, and the overall reaction becomes the direct methane oxidation. Mention that the fluctuations reflected in the data presented in Figs. 9 and 10 could be due to the electrical interferences caused by the proximity of electrical cables (load and voltage) and the oven, increasing at higher temperature.

The IV curves and Nyquist diagrams measured after the endurance tests are illustrated in Fig. 11. The maximum power densities achieved were 163, 205 and 371 mW cm^{−2} at 750, 800 and 850 °C, respectively. It can be observed that these values are slightly higher compared to initial measurement in identical experimental conditions (Table 1). The impedance data of Fig. 11b were also fitted to equivalent circuit proposed before. Similar resistances values were obtained which indicate no carbon deposition on the anode material. EDX analyses of the cell anode after the operation also confirmed the absence of carbon deposits.

4. Conclusions

MoNi–Ce has been synthesized by coprecipitation within reverse microemulsion and examined its catalytic and electrochemical properties as anode material for SOFC. An 12.8% conversion for methane oxidation was observed at 850 °C and the carbon deposited over the sample had low graphitization degree suggesting its easy elimination. The electrochemical performance of

MoNi–Ce anode in a single SOFC cell using LSGM as electrolyte and fed by different humidified fuels (H_2 , CH_4 and H_2/CH_4 mixtures) and static air as oxidant has been evaluated at 750, 800 and 850 °C. The electrochemical results evidenced that the cell performance was stable in all studied gas compositions. The power output of this cell improved with increasing temperature and decreasing CH_4 content in the gas feeding. The open circuit voltages showed that the anode material presented activity catalytic for partial oxidation of CH_4 which enhanced with the temperature. The impedance analysis revealed that the low frequency arc, associated with the anode, was larger with the increase of methane content in the fuel. In addition, no deterioration of the cell performance was detected when was running in pure CH_4 under a constant current density for 10 h at each studied temperature. Then, MoNi–Ce compound exhibited a good tolerance to carbon deposition when was operated in wet pure CH_4 at high current density and could be a promising anode material for direct oxidation of methane.

Acknowledgements

This work was supported by Spanish Ministry of Economic and Competitiveness (MAT2010-20846) and the Community of Madrid (DIVERCEL; Ref.S009/ENE-1475).

References

- [1] C. Sun, U. Stimming, *J. Power Sources* 171 (2007) 247–260.
- [2] X. Sun, S. Wang, Z. Wang, J. Qian, T. Wen, F. Huang, *J. Power Sources* 187 (2009) 85–89.
- [3] C. Lu, W.L. Worrell, R.J. Gorte, J.M. Vohs, *J. Electrochem. Soc.* 150 (3) (2003) A354–A358.
- [4] Z.H. Bi, J.H. Bu, *J. Power Sources* 195 (2010) 3097–3104.
- [5] A. Fuerte, R.X. Valenzuela, M.J. Escudero, L. Daza, *J. Power Sources* 196 (2011) 4324–4331.
- [6] S. Tao, J.T.S. Irvine, *J. Electrochem. Soc.* 151 (2) (2004) A252–A259.
- [7] S.P. Jiang, X.J. Chen, S.H. Chan, J.T. Kwok, K.A. Khor, *Solid State Ionics* 177 (2006) 149–157.
- [8] V.V. Kharton, E.V. Tsipis, I.P. Marozau, A.P. Viskup, J.R. Frade, J.T.S. Irvine, *Solid State Ionics* 178 (2007) 101–113.
- [9] Y.H. Huang, R.I. Dass, Z.L. Xing, J.B. Goodenoughs, *Science* 312 (2006) 254–257.
- [10] Z. Wang, Y. Tian, Y. Li, *J. Power Sources* 196 (2011) 6104–6109.
- [11] P. Zhang, Y.H. Huang, J.G. Cheng, Z.Q. Mao, J.B. Goodenough, *J. Power Sources* 196 (2011) 1738–1743.
- [12] J.B. Wang, J.C. Jang, T.J. Huang, *J. Power Sources* 122 (2003) 122–131.
- [13] S.M. Bukhari, J.B. Giorgi, *J. Power Sources* 198 (2011) 51–58.
- [14] C. Xu, J.W. Zondlo, M. Gong, F. Elizalde-Blancas, X. Liu, I.B. Celik, *J. Power Sources* 195 (2010) 4583–4592.
- [15] J. Qiao, K. Sun, N. Zhang, B. Sun, J. Kong, D. Zhou, *J. Power Sources* 169 (2007) 253–258.
- [16] Y.H. Huang, R.I. Dass, Z.L. Xing, J.B. Goodenough, *J. Electrochem. Soc.* 158 (2011) B605–B613.
- [17] M. Liu, G. Wei, J. Luo, A.R. Sanger, K.T. Chuang, *J. Electrochem. Soc.* 150 (2003) A1025–A1029.
- [18] M.J. Escudero, I. Gómez de Parada, A. Fuerte, L. Daza, in: *Proceedings of 10th European Solid Fuel Cell Forum, European Fuel Cell Forum AG, Luzern (Switzerland)*, 2012, p. B0426.
- [19] J.H. Wan, J.Q. Yan, J.B. Goodenough, *J. Electrochem. Soc.* 152 (8) (2005) A1511–A1515.
- [20] P. Burroughs, A. Hamnett, A.F. Orchard, G. Thornton, *J. Chem. Soc. Dalton Trans.* (1976) 1686–1698.
- [21] C. Larese, M. López Granados, R. Mariscal, J.L.G. Fierro, P.S. Lambrou, A.M. Efsthathiou, *Appl. Catal. B* 59 (2005) 13–25.
- [22] A. Siokou, S. Ntais, V. Dracopoulos, S. Papaefthimiou, G. Leftheriotis, P. Yianoulis, *Thin Solid Films* 514 (2006) 87–96.
- [23] K.A. Gesheva, T. Ivanova, B. Marsen, B. Cole, E.L. Miller, F. Hamelmann, *Surf. Coat. Technol.* 201 (2007) 9378–9384.
- [24] M.W. Tan, E. Akiyama, A. Kawashima, K. Asami, K. Hashimoto, *Corros. Sci.* 38 (1996) 1495–1511.
- [25] L. Soriano, I. Preda, A. Gutiérrez, S. Palacín, M. Abbate, A. Vollmer, *Phys. Rev. B Condens. Matter.* 75 (2007) 233417–1–233417-4.
- [26] N.S. McIntyre, M.G. Cook, *Anal. Chem.* 47 (1975) 2208–2213.
- [27] J. Abart, E. Delgado, G. Ertl, H. Jeziorowski, H. Knozinger, N. Thiele, X.Zh. Wang, *Appl. Catal. B* 2 (1982) 155–176.
- [28] W. Wang, R. Ran, Z. Shao, *Int. J. Hydrogen Energy* 36 (2011) 754–764.
- [29] D.L. Trimm, *Catal. Today* 37 (1997) 233.
- [30] J. Sfeir, P.A. Buffat, P. Möckli, N. Xanthopoulos, R. Vasquez, H.J. Mathieu, J. Van Herle, K.R. Thampi, *J. Catal.* 202 (2001), 229–244.
- [31] W. Guo, J. Liu, Y. Zhang, *Electrochim. Acta* 53 (2008) 4420–4427.
- [32] Y. Li, S.A. Barnett, *Electrochem. Solid-State Lett.* 9 (6) (2006) A285–A288.
- [33] V.V. Khartona, A.P. Viskup, A.A. Yaremchenko, R.T. Baker, B. Gharbage, G.C. Mather, F.M. Figueiredo, E.N. Naumovich, F.M.B. Marques, *Solid State Ionics* 132 (2000) 119–130.
- [34] T. Ishihara, T. Shibayama, M. Honda, H. Nishiguchi, Y. Takita, *J. Electrochem. Soc.* 147 (4) (2000) 1332–1337.
- [35] K. Kendall, C.M. Finnerty, G. Saunders, J.T. Chung, *J. Power Sources* 106 (2002) 323–327.
- [36] J. Liu, S.A. Barnett, *Solid State Ionics* 158 (2003) 11–14.
- [37] J. Canales-Vázquez, J.C. Ruiz-Morales, J.T.S. Irvine, W. Zhou, *J. Electrochem. Soc.* 152 (7) (2005) A1458–A1465.
- [38] B. Huang, X.F. Ye, S.R. Wang, H.W. Nie, J. Shi, Q. Hu, J.Q. Qian, X.F. Sun, T.L. Wen, *J. Power Sources* 162 (2006) 1172–1181.
- [39] F. Mauvy, C. Lalanne, J.M. Bassat, J.C. Grenier, H. Zhao, L. Huo, P. Stevens, *J. Electrochem. Soc.* 153 (2006) A1547–A1553.
- [40] M. Rieu, R. Sayers, M.A. Laguna-Bercero, S.J. Skinner, P. Lenormand, F. Ansart, *J. Electrochem. Soc.* 157 (4) (2010) B477–B480.
- [41] J.T.S. Irvine, D.C. Sinclair, A.R. West, *Adv. Mater.* 2 (1990) 132–138.
- [42] M. Brown, S. Primdahl, M. Mørgersen, *J. Electrochem. Soc.* 147 (2) (2000) 475–485.
- [43] P. Vernoux, M. Guillo, J. Fouletier, A. Hammou, *Solid State Ionics* 135 (2000) 425–431.
- [44] D. Kek, M. Morgenson, S. Pejovnik, *J. Electrochem. Soc.* 148 (8) (2001) A878–A886.
- [45] Q.X. Fu, D. Stöver, *J. Electrochem. Soc.* 153 (4) (2006) D74–D83.
- [46] M. Chen, B.H. Kim, Q. Xu, B.G. Ahn, D.P. Huang, *Solid State Ionics* 181 (2010) 1119–1124.
- [47] Y. Lin, Z. Zhan, J. Liu, S.A. Barnett, *Solid State Ionics* 176 (2005) 1827–1835.
- [48] M.A. Buccheri, A. Singh, J.M. Hill, *J. Power Sources* 196 (2011) 968–976.